

## T.2: Imaging crystal growth process and investigating optical properties and defects structure of crystals

Sunil Verma

*Optical Composite Materials Lab.*

*Laser and Functional Materials Division*

*Email: sverma@rrcat.gov.in*

### Abstract

Crystals are driving the current photonics revolution. Material scientists need to have a detailed understanding of how crystals grow, whereas device engineers need crystals of adequate size and quality for the end applications. Growth rate and defect structure of a crystal is a function of the time-dependent spatial distribution of the temperature, convection and concentration profiles during crystal growth process, therefore it is important to map these transport processes and understand their influence on the growing crystal. The first part of the present article discusses the optical techniques developed and the results obtained during online and *in situ* optical imaging of the crystal growth process. Post-growth, the grown crystal is cut and polished along specific directions to obtain the element for use in the desired device. However, before deploying a crystal element for a particular application, it is necessary to assess its optical quality and measure important optical properties. The second part of the article discusses various optical and x-ray techniques used for investigating the optical properties and defects structure of the crystals.

### 1. Introduction

The process of crystal growth from solution is simultaneously influenced by several internal and external factors [1]. The former includes the crystal structure while the latter includes various physico-chemical parameters such as the nature of the solvent, the hydrodynamic conditions, the heat and mass transfer processes. These parameters have a complex relationship with the defects structure, hence the quality of the growing crystal, therefore mapping of these parameters during growth is a useful experimental approach for understanding the process of crystal growth and regulating growth conditions to produce crystals of desired size and quality [2, 3]. Optical imaging techniques are used for the purpose, which have several advantages such as they do not affect the process under study, their response is inertia-free and provide full-field information of the process [4, 5].

The crystal growth process is a non-equilibrium process and therefore several defects get incorporated in the crystal during growth. Correlating the defects state of the crystal with their optical properties is an important research area having implications for the device applications of the crystal. In this

direction, concerted efforts have been made resulting in establishing several experimental facilities for the purpose, in particular, interferometric set up for investigating the refractive index homogeneity, UV-Vis-NIR spectrophotometry for estimating the bulk transmittance, two-wave coupling experiment for measuring photorefractive properties and Z-scan for 3<sup>rd</sup> order NLO properties. The correlation between the optical properties and defects structure of the crystal has been specifically investigated by mapping the defects structure using x-ray topography, high-resolution x-ray diffraction (HRXRD) and x-ray fluorescence studies.

### 2. Optical imaging of crystal growth process

#### 2.1 Imaging convection during crystal growth using laser shadowgraphy

Shadowgraphy is based on the principle of refraction of light rays when they encounter varying refractive index field in their path [6]. Laser shadowgraphy was used for mapping free convection phenomenon during growth of potassium dihydrogen phosphate (KDP) crystal [7, 8]. Since the change of solution density with temperature ( $dp/dT$ ) is negative and that with solute concentration ( $dp/dC$ ) is positive, the density fields are set up in the crystallizer. These density fields prevalent around the crystal were observed in the form of rising buoyant convection plumes. With the passage of time, crystal size increases and the flow pattern was observed to undergo transition from being laminar to chaotic (Figure T.2.1). The flow field intermittently becomes oscillatory and unstable, and modifies the concentration gradient along the growth interface. As a result, the growth rate and quality of the crystal are a function of the time-dependent spatial distribution of the convection patterns and of the concentration profiles around it.

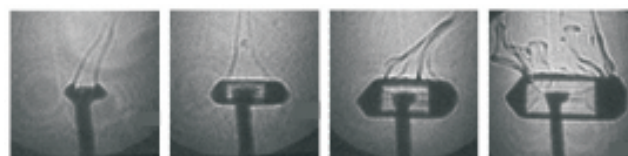


*Fig. T.2.1: Shadowgraph images showing the flow transition from laminar to irregular and finally chaotic.*

The strength of free convection as observed in the shadowgraph images was estimated in terms of Grashof number. It was observed that beyond a critical value of this number the free convection activity becomes very vigorous, and the crystal quality becomes sensitive to fluctuation in the concentration field (Figure T.2.2a). This critical Grashof number falls within 50 to 80 for a crystal growing on top of a glass rod [9]. Inclusions and striations were found to get incorporated beyond this stage. The time-lapsed shadowgraph images were also used to quantify the growth

rate as a function of supercooling (Figure T.2.2b). The shadowgraph images during growth of KDP under free convection conditions were also used to identify signatures of growth mechanisms. Two growth mechanisms namely, layer-by-layer growth and 3D cluster growth were observed [10]. The boundary layer thickness was estimated for various habit faces of the crystal and found to be intricately linked to the growth kinetics. Thinner the boundary layer, faster was the growth kinetics.

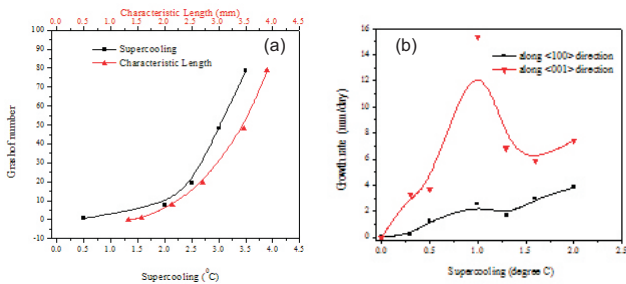


Fig. T.2.2: (a) Strength of free convection quantified in terms of Grashof number; (b) Growth rates along <100> and <001> directions of KDP crystal.

Time-lapsed shadowgraphy was also used to investigate polar morphology of Zinc Tris (thiourea) Sulphate NLO crystals (Figure T.2.3). The growth rates of {010} and {001} faces as a function of supersaturation were computed (Figure T.2.4) and the anisotropy was explained on the basis of chemical environments on the two sides of (001) slice [11].

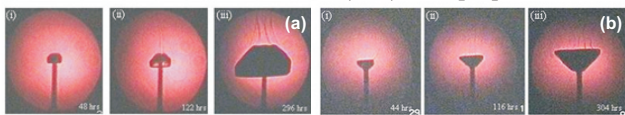


Fig. T.2.3: Shadowgraphy of ZTS growth with (a) (001) face upward and (b) (00-1) face upward.

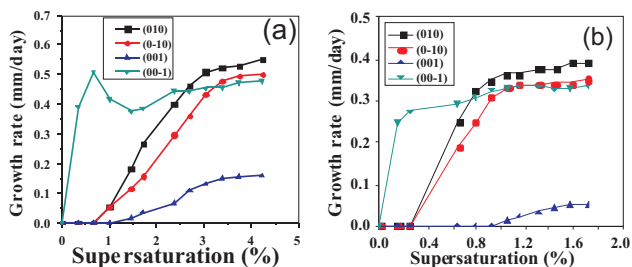


Fig. T.2.4: Growth rates of ZTS crystal with (a) (001) face upward and (b) (00-1) face downward.

### 2.2 Imaging crystal surface micromorphology using Michelson interferometry

Michelson interferometry is a useful technique for mapping of micromorphology of habit faces of a growing crystal [12]. Here, one of the interfering beams was reflected from the

surface of a growing crystal, which interfered with a reference beam reflected from a mirror to generate an interferogram that carried information of the microtopography of the growing crystal surface. The phase variation due to growth or dissolution of the crystal surface manifests itself in the form of change in the fringe pattern. Whenever the crystal thickness changes by  $\lambda/2n$ , one fringe shift takes place, where  $\lambda$  is the wavelength of the laser used and  $n$  is the refractive index of the solution. Quantitative analysis of the interferogram yields various growth-kinetic parameters. The height difference between two points on adjacent fringes is

$$d = \frac{\lambda}{2n}$$

given by  $d = \frac{\lambda}{2n}$ . If the total variation in the crystal thickness normal to the crystal face is  $\Delta h$  in time  $\Delta t$ , the normal average growth rate is given by  $R = \frac{\Delta h}{\Delta t}$ . Here,  $\Delta h = N \times d$ , where  $N$  is

the total number of fringes that have crossed the point of observation on the interferogram. Thus the normal average

$$R = \frac{N \times \lambda}{2 \times n \times \Delta t}$$

growth rate becomes  $R = \frac{N \times \lambda}{2 \times n \times \Delta t}$ . If  $D$  is the physical distance

between the two points lying on adjacent fringes, the slope  $p$  of the hillock is given by  $p = \tan \theta = \frac{d}{D}$ . The normal growth

rate and the slope of the dislocation hillock are related to the tangential step velocity  $V$  as  $R = p \times V$ . Using this technique

surface micromorphology of prismatic and pyramidal faces of the KDP crystal has been imaged. Screw dislocation mediated spiral growth mechanism has been imaged in the form of concentric fringes of equal thickness over the (100) KDP habit face (Figure T.2.5). The normal and tangential growth rates computed from the interferograms were  $2.32 \times 10^{-5}$  mm/min and  $2.5 \times 10^{-2}$  mm/min respectively. The slope of the dislocation hillock in Figure T.2.5 was  $9.28 \times 10^{-4}$  [10].

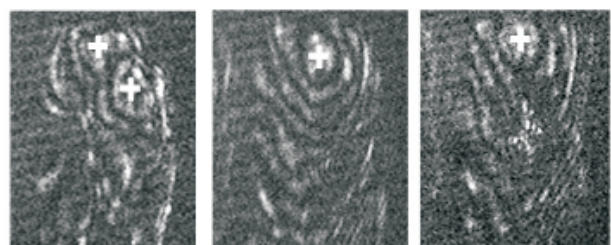


Fig. T.2.5: Michelson interferogram due to screw dislocation mediated spiral growth mechanism. The position of the dislocations is marked by '+'.

### 2.3 Imaging of concentration gradient during crystal growth using Mach-Zehnder interferometry

A rhomboid prism based Mach-Zehnder interferometer was developed for studying heat and mass transfer processes during crystal growth (Figure T.2.6). This interferometer was immune to frequent misalignment due to external vibrations and fluctuations in ambient conditions.

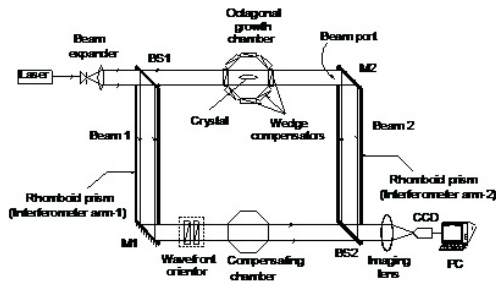


Fig. T.2.6: Schematic of rhomboid prism based Mach-Zehnder interferometer for crystal growth studies.

A parametric study was performed to optimize the forced flow conditions such that the concentration inside the crystallizer was uniform throughout the growth experiment [13]. Figure T.2.7 shows the infinite fringe interferogram of concentration during crystal growth under varying forced flow conditions.

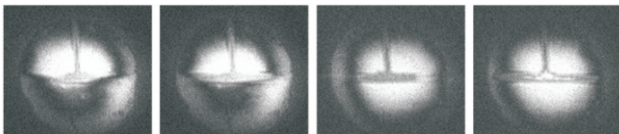


Fig. T.2.7: M-Z interferograms of concentration field during different forced convection conditions.

The Mach-Zehnder interferometer was also deployed for *in situ* and on-line measurement of concentration during free convection growth [10]. Figure T.2.8 shows time lapsed Mach-Zehnder interferograms of the concentration gradient developing inside the crystallizer during KDP crystal. Such a gradient is detrimental to growth of a good quality crystal as the inclusions get incorporated in the crystal at this stage. Additionally, the growth of the crystal became anisotropic due to varying concentration levels along the length of the crystal. Therefore a Mach-Zehnder interferometer is a useful diagnostic for on-line monitoring of the concentration field.



Fig. T.2.8: Progressive stages of concentration gradient during free convection growth of KDP crystal.

### 2.4 Simultaneous imaging of concentration and surface features using double Mach-Zehnder interferometry

A double Mach-Zehnder interferometer has been developed for simultaneous imaging of the concentration field around the crystal and the surface microstructure on the crystal faces during growth from solution [14]. It has an outer MZ interferometer which maps the concentration distribution near the growing crystal. The outer unit envelops an inner MZ interferometer that records the surface features on the habit face of the growing crystal (Figure T.2.9). The crystal is suitably oriented so that the face whose surface kinetics is to be studied is at 45° to the incoming light direction. The light beam reflected from the crystal surface forms the test beam for the inner MZ interferometer, which upon superposition with the reference beam generates dynamic interference pattern of the time-dependent microscopic features developing over the crystal surface. The unblocked light beam traversing through the solution becomes the test beam of the outer MZ interferometer. It carries information of the fluid around the crystal and upon interference with the test beam yields information about the concentration field. A benchmark experiment with a prismatic face of KDP crystal was performed using this interferometer by aligning the outer MZ interferometer in wedge fringe mode and the inner interferometer in infinite-fringe mode. Figure T.2.10 shows composite interferograms. As the crystal grows, the wedge fringes, initially straight, develop curvature adjacent to the crystal faces. The slope of these fringes are proportional to the concentration gradient while the displacement is a measure of the change in concentration. The inner MZ interferometer shows appearance of concentric fringes, each representing location of the growth hillock. Changes in these images with time reveal time-dependent growth phenomena.

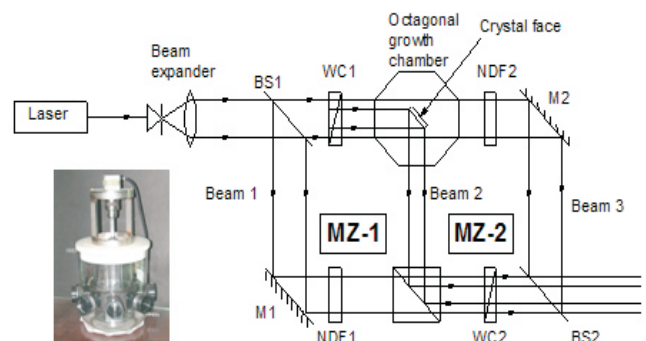


Fig. T.2.9: Optical schematic and growth chamber for double M-Z interferometer studies.

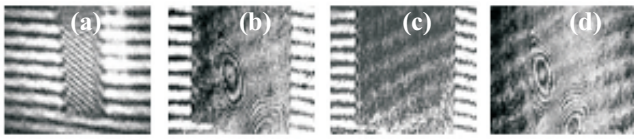


Fig. T.2.10: (a) Double M-Z composite interferogram when both the interferometers are set in wedge modes; (b) the outer interferogram represents the solution characteristics and the inner interferogram (circular fringes) represents the surface features; (c) fringes in the solution as well as at the crystal boundary when beam-2 is blocked; (d) only the surface features are observed when beam-3 is blocked.

### 2.5 Quantifying thermal and concentration driving forces simultaneously during crystal growth using dual-wavelength Mach-Zehnder interferometry

During crystal growth from solution, mass transfer from the bulk solution to the growing crystal is achieved via thermal processes of cooling or evaporation. In order to quantify thermal and concentration driving forces simultaneously at a given stage of growth, dual-wavelength interferometric diagnostic has been developed [15]. The total change in refractive index for a process influenced simultaneously by the temperature and the concentration fields is

$$\Delta n = \frac{\partial n}{\partial C} \Delta C + \frac{\partial n}{\partial T} \Delta T$$

Taking into account the wavelengths ( $\lambda_1$  and  $\lambda_2$ ), the length (L) of the process chamber and the number of fringes passing the point of observation in the respective interferogram ( $N_1$  and  $N_2$ ), the above equation for the two wavelengths can be written as [16]

$$\frac{N_1 \lambda_1}{L} = \left( \frac{\partial n}{\partial C} \right)_{\lambda_1} \Delta C + \left( \frac{\partial n}{\partial T} \right)_{\lambda_1} \Delta T$$

$$\frac{N_2 \lambda_2}{L} = \left( \frac{\partial n}{\partial C} \right)_{\lambda_2} \Delta C + \left( \frac{\partial n}{\partial T} \right)_{\lambda_2} \Delta T$$

The LHS of above equations have experimental parameters (L,  $\lambda$  and fringe numbers), while the RHS has the solution properties (refractive index gradients w.r.t. T and C at  $\lambda_1$  and  $\lambda_2$ ). Solving these equations simultaneously, we get  $\Delta T$  and  $\Delta C$  [17].

As a case study, the technique has been implemented during crystal growth of triglycine sulphate (TGS). The M-Z interferograms recorded at three stages of growth corresponding to the cooling of solution by 1, 3 and 6 °C are shown in Figure T.2.11(a-c) respectively. The refractive index is obtained using the Cauchy equation and the refractive index gradients with respect to T and C are obtained using Murphy-Alpert and Lorentz-Lorenz relationship [18], respectively and the fringes passing the field of view are obtained by dual-wavelength M-Z interferometry. Table T.2.1 shows the quantified thermal and concentration driving forces at the three stages of growth. The measured driving forces

approximately follow the solubility data of TGS. The difference between the measured and actual driving forces could be attributed to the consumption of solute in crystal growth and minor fringe counting errors.

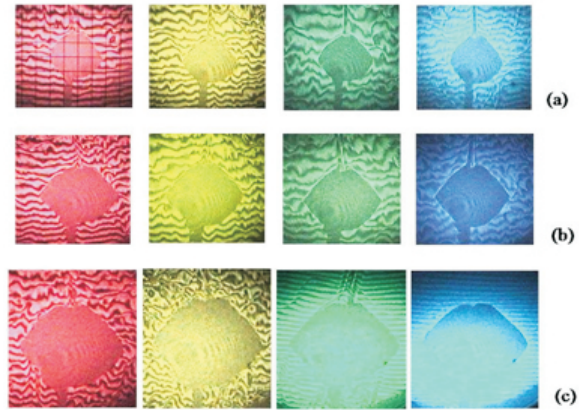


Fig. T.2.11: Mach-Zehnder interferograms recorded using 6470, 5680, 5140 and 4880 Å wavelengths during TGS crystal growth corresponding to the cooling of (a) 1, (b) 3 and (c) 6 °C, respectively.

Table T.2.1: Thermal and concentration driving forces at the three stages of TGS crystal growth experiment.

Growth stage	Fringe number passing the point of observation		Measured concentration driving force ( $\Delta C$ ) gm TGS/litre water	Measured thermal driving force ( $\Delta T$ ) i.e. supercooling (in degree)	Actual thermal driving force (supercooling during growth)
	$N_1$ ( $\lambda_1 = 6470 \text{Å}$ )	$N_2$ ( $\lambda_2 = 4880 \text{Å}$ )			
Initial	25	34	6.12	0.8	1.0
Intermediate	81	110	16.46	2.6	3.0
Last stage	169	230	44.81	5.4	6.0

### 2.6 Tomographic reconstruction of convective and concentration fields during crystal growth

The limitation of shadowgraphy and interferometry is that they provide two-dimensional images of parameters such as concentration and convection which are actually three dimensional in nature. Therefore, in order to get a complete understanding of these fields, it is necessary that the 2D data obtained through shadowgraphy and interferometry is converted to 3D information. This is possible through the use of computerized tomography [19]. In the context of the present study, the projection data is in the form of line integrals of the refractive index field around the growing crystal. These manifest as intensity values in the shadowgraph images and the fringes in the Mach-Zehnder interferograms. These are then used to generate three dimensional maps of either concentration or convective features above the growing crystal.

Tomography is implemented in two-steps. (1) Collect projection data using an appropriate optical technique; (2) Reconstruct the desired field parameter using numerical algorithms such as the *convolution back projection (CBP)* [20] or the *algebraic reconstruction technique (ART)* [21].

The above principles were implemented during KDP crystal growth for 3D reconstruction of concentration and convective features using shadowgraph projection data [22, 23]. Convective features as seen in the shadowgraph images were reconstructed over three planes at different heights above the crystal. The CBP and ART reconstruction algorithms were used for the purpose. Three different data types namely, intensity values, contrast ( $I_o - I_s / I_s$ ), and refractive index corresponding to each shadowgraph image was used for reconstruction. Figure T.2.12(a-c) shows the three types of projection data for a shadowgraph image. The tomographically reconstructed contour plots using light intensity as the projection data are shown in Figure T.2.13. The results indicated that ART algorithm was able to reconstruct the broad features in the shadowgraph images with the 18 view data-set. The fine features appeared when a finer data-set of 90 views was used. The contour plots of the intensity based reconstruction brought out the fact that the rising plumes spread horizontally as they move up into region of low concentration. The shape of the plume has bearing on the stability of convection and hence on the quality of the growing crystal. The gradients were seen to be high in the region just above the crystal, while they were smoother in the bulk of the crystallizer. Tomographic imaging proved to be a useful diagnostic to obtain three dimensional character of the convection (and hence concentration).

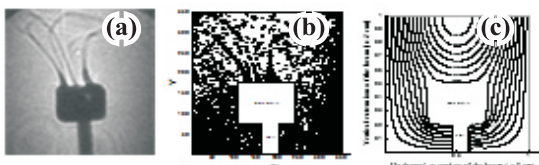


Fig. T.2.12: Three types of projection data corresponding to the shadowgraph image. (a) Intensity, (b) contrast, and (c) refractive index.

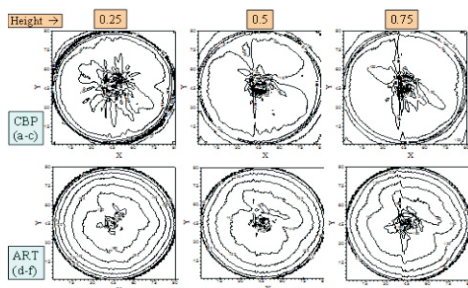


Fig. T.2.13: Tomographic reconstruction of the convective field over a horizontal plane above a growing crystal at different heights.

### 3. Optical characterization of crystals

In this section various techniques set up or used for measuring the device relevant optical properties of the grown crystal are discussed.

#### 3.1 UV-Vis-NIR transmittance of crystals

Transmission studies provide information about the bulk optical quality of the crystal and the spectral range within which the crystal could be used for device applications. KDP crystal grown along [001] direction as well as along phase matching directions were investigated for their transmittance [24, 25]. Four plates, each of 1 mm thickness and oriented along (100) and (001) from top and bottom regions of the KDP crystal grown along [001] direction, were taken for the transmission studies. Similarly, two plates, one from the top and other bottom of the SHG oriented KDP crystal were also taken for investigations [26]. Figure T.2.14(a, b) shows the transmission spectra of these plates. The transmittance in the visible region without accounting for the Fresnel reflection was ~90% for all the four plates with negligible variation. The transmittance in UV region for all the plates was less compared to visible region. However, transmittance decreases drastically for *a*-cut plate taken from the bottom of the crystal. This is attributed to the absorption of UV by the trivalent impurities ( $Al^{3+}$ ,  $Fe^{3+}$ ,  $Cr^{3+}$  etc.), which are predominantly present in the prismatic sector (lower part of the crystal) as compared to the pyramidal sector (upper part) of the KDP crystal. Similar results have been obtained for samples taken from flat-top KDP crystal [27].

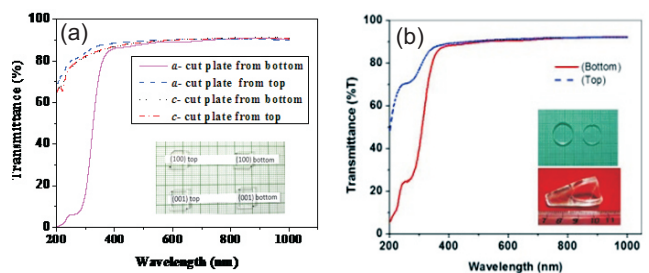


Fig. T.2.14: Transmission of plates taken from (a) KDP crystal grown along [001] direction and (b) KDP grown along phase matching direction.

#### 3.2 Investigating optical indicatrix of crystals using conoscopy

Conoscopic interferometry is performed to get information about the homogeneity of the crystal and its optical indicatrix. When a converging beam of white light, polarized along a specific direction, is passed through the crystal plate, the beam splits into *e*- and *o*-rays. The phase difference between the two rays is

$$\delta = \frac{2\pi d}{\lambda \cos\theta} (n_e - n_o)$$

where  $d$  is the thickness of the sample,  $n_e$  and  $n_o$  are the refractive indices of  $e$  and  $o$  rays respectively, and  $\theta$  is the angle of refraction. The emerging rays are made to recombine along the axis of an analyzer. This results in concentric fringes of interference colors (isochromes) and a black cross (isogyres) with dark spot in the centre (melatope). Figure T.2.15(a, b) shows the conoscopic patterns for double doped  $\text{LiNbO}_3$  and KDP crystals grown in the Lab [26, 28, 29]. First image in each is along the optic axis of the sample and the second is obtained when a retardation plate is introduced to find the sign of optic axis. The symmetrical fringe pattern represents good optical homogeneity of the crystal. In order to determine the sign of the optic axis, a wave plate (530 nm) was introduced at  $45^\circ$  to the polarizer and between the crystal plate and the analyzer. It results in change in the interference colors of the four quadrants of the image, which are compared with the interference color chart to infer about the sign of optic axis of the crystal.

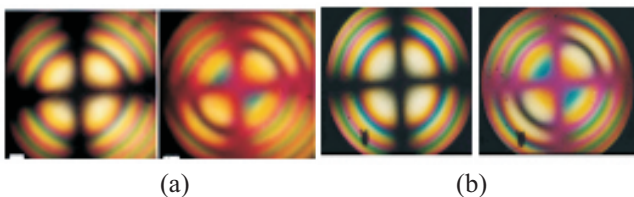


Fig. T.2.15: Conoscopic patterns for (a)  $\text{Fe:Mn:LiNbO}_3$  and (b) KDP crystal. First image in each is along the optic axis and the second when a retardation plate is introduced to find the sign of optic axis.

Investigations of optical indicatrix of an optically biaxial crystal such as zinc tris (thiourea) sulphate (ZTS) crystal were also carried out using conoscopy [30]. Its optical indicatrix is an ellipsoid with three different principal refractive index axes. The two optic axes are symmetrical about the  $Z$  axis (or  $n_z$ -axis) and the angle between the two is called optic angle or  $2V_z$  angle. The interference pattern obtained when the acute bisectrix is oriented perpendicular to the microscope stage is shown in Figure T.2.16a. The melatopes lie outside the field of view of the conoscopic image, which happens when the  $2V_x$  angle is large. The isochromes surround the melatope on the left and right edges of the image. The isogyres coincide with the crosshairs of the microscope. On rotating the microscope stage by  $45^\circ$ , the melatope cross splits and the isogyres form two hyperboles that lie in the opposite quadrants of the conoscopic image (Figure T.2.16b). When the crystal plate is oriented such that one of the optic axes is perpendicular to the microscope stage, circular isochromes are visible along with single isogyres in the conoscopic image (Figure T.2.16c). When a wave plate was inserted (530 nm), the interference colors were found to increase due to addition of path difference (Figure T.2.16d). The characteristic changes in the

interference color of the conoscopic image confirm that the crystal is optically negative.

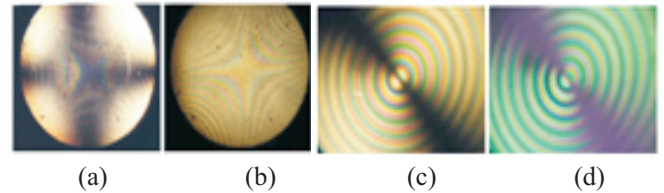


Fig. T.2.16: Conoscopic of ZTS crystal plates.

### 3.3 Assessing the optical quality of the crystals using birefringence interferometry

Birefringence interferogram gives cumulative information about all those defects which influence the birefringence of the crystal. When an expanded and collimated beam of wavelength is polarized such that the plane of polarization of the incident beam makes an angle of  $45^\circ$  with the optic axis of the crystal element (thickness  $L$  and cross-sectional aperture  $W$ ), each ray splits into  $e$ - and  $o$ - components of equal amplitudes in the crystal sample. These components traverse through the crystal element and at the exit face emerge with a definite path difference. The components of  $e$ - and  $o$ - rays along the analyzer axis interfere to produce an interference pattern referred to as the birefringence interferogram. The phase difference between the interfering  $e$ - and  $o$ - components is [28]

$$\phi = \frac{2\pi}{\lambda} \times \left\{ [L \times (n_e - n_o)] + [L \times \Delta(n_e - n_o)] + [\Delta L \times (n_e - n_o)] \right\}$$

The first term on the right is the phase difference arising due to the birefringence of the crystal, the second term is the phase difference arising due to the variation of birefringence across the sample cross-section and the third term is the phase difference arising due to the variation in the sample thickness across its cross-section. Usually a crystal element has different types of defects, which invariably results in change in the refractive indices across its cross-section, and hence variation in the sample birefringence. As a result the birefringence interferogram has several fringes depending upon the extent of variation in the birefringence. By counting the number of fringes in the interferogram, the total variation in the birefringence,  $\Delta(n_e - n_o)$ , across the cross-section of the crystal element can be quantified. Further, the shape of the fringe provides us the information that whether the birefringence is periodically varying or random across the sample cross-section. The variation in birefringence,  $\Delta(n_e - n_o)$ , is given by  $\Delta(n_e - n_o) = N\lambda/L$ , where  $N$  is the number of interference fringes observed using laser beam of diameter  $D$  and wavelength  $\lambda$  after passing through a crystal plate of uniform thickness  $L$ . Therefore, linear gradient of birefringence of the sample normal to fringes was calculated

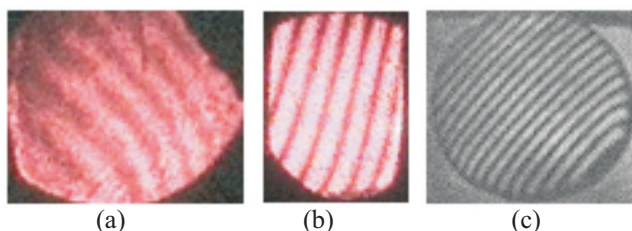


Fig. T.2.17: Birefringence interferogram for (a) Fe:LiNbO<sub>3</sub> crystal, (b) Mn:Li<sub>2</sub>B<sub>4</sub>O<sub>7</sub> crystal, and (c) KDP crystal.

using formula,  $N\lambda/LD$ . A few examples of the use of this interferometer for the above application are shown in Figure T.2.17(a-c). The variation in birefringence for a plate of Fe:LiNbO<sub>3</sub> crystal of size 10×10×2 mm<sup>3</sup> was found to be 0.001898 [31], for a Mn:Li<sub>2</sub>B<sub>4</sub>O<sub>7</sub> crystal plate of size 10×6×1 mm<sup>3</sup> was 0.003894 [32], and KDP plate normal to the phase matching direction of size 10 mm dia.×1.34 mm thickness was 0.00753 [26].

### 3.4 Refractive index homogeneity of crystals using Mach-Zehnder interferometry

The Mach-Zehnder interferometer aligned in infinite fringe mode was used to test the crystal element for refractive index inhomogeneities. The samples were made in the form of parallel plates and the surfaces were polished to make them optically flat and parallel to each other. It may be pointed out that in addition to the local inhomogeneities in the sample, one can also get an estimate of the wedge angle. This is a crucial parameter when the element being tested has end application where the wedge angle desired is almost zero, such as elements required for disc laser applications. Figure T.2.18(a,b) show the Mach-Zehnder interferogram for two samples of lithium tetra borate crystal [33]. Ideally, under the conditions of no inhomogeneities and no wedge angle, the interferogram should have only one fringe. However, as shown in Figure T.2.18a, there are a large number of parallel and equispaced fringes representing that the sample has a good overall homogeneity but has a wedge formed by the opposite surfaces. However, zooming down to individual fringes shows fringe irregularities at microscopic level, which could be attributed to local refractive index inhomogeneities.

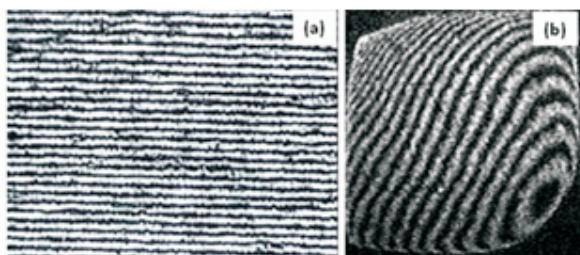


Fig. T.2.18: Mach-Zehnder interferogram for samples of Lithium Tetra Borate crystal.

Figure T.2.18b shows the fringe pattern for the second sample. In this case the fringes are irregularly spaced and are curved at the edges, indicating inhomogeneities in the sample as well as that the sample surfaces are curved at the edges due to polishing errors. Quantitative analysis of the interferogram shows that the refractive indices variations are  $\sim 10^{-5}$ . Similar studies have been performed for several inorganic and organic NLO crystals grown in the Lab [26-28, 30, 33-34].

### 3.5 Investigating NLO properties of crystals using Z-scan technique

Z-scan is widely used for material characterization because it provides not only the magnitudes of the real and imaginary parts of the 3<sup>rd</sup> order nonlinear optical susceptibility, but also the sign of the real part [35]. There are two types of the Z scan, namely "closed aperture" and "open aperture". Closed aperture configuration is helpful for finding out nonlinear refractive index coefficient while open aperture configuration is for nonlinear absorption coefficient. Nonlinear refractive index ( $n_2$ ) is calculated as

$$n_2 = \frac{\Delta T_{p-v} \times \lambda}{0.406(1-S)^{0.25} \times 2\pi \times I_o \times L_{eff}}$$

where  $\Delta T_{p-v}$  is difference between the peak and valley transmittance values,  $L_{eff}$  is effective thickness of a sample and S is linear aperture that lies between 0 to 1, where 0 means fully closed aperture and 1 means fully open aperture. Nonlinear absorption coefficient ( $\beta$ ) is calculated as

$$\beta = \frac{2\sqrt{2} \times \Delta T}{I_o \times L_{eff}}$$

where  $\Delta T$  is difference between the highest and lowest values of the normalized open aperture transmittance curve. Real and imaginary components of the 3<sup>rd</sup> order optical susceptibility are obtained by:

$$\text{Re}\chi^{(3)}(esu) = \frac{10^{-4} \epsilon_o c^2 n_o^2 n_2 (cm^2/W)}{\pi}$$

$$\text{Im}\chi^{(3)}(esu) = \frac{10^{-4} \epsilon_o c^2 n_o^2 \lambda \beta (cm/W)}{4\pi^2}$$

Absolute value of 3<sup>rd</sup> order optical susceptibility is

$$|\chi^{(3)}| = \sqrt{(\text{Re}\chi^{(3)})^2 + (\text{Im}\chi^{(3)})^2}$$

Z-scan studies were performed for several inorganic and organic crystals grown in the Lab. The representative results for LiNbO<sub>3</sub> and LTB crystals are shown in Figure T.2.19 and Table T.2.2 [36].

Table T.2.2: Measured  $n_2$  and  $\beta$  values.

Crystal	$n_2$ (cm <sup>2</sup> /W)	$\beta$ (cm/W)
Lithium Niobate	$3.04 \times 10^{-7}$	$2.1 \times 10^{-2}$
Lithium Tetra Borate	$9.8386 \times 10^{-8}$	$1.0 \times 10^{-3}$

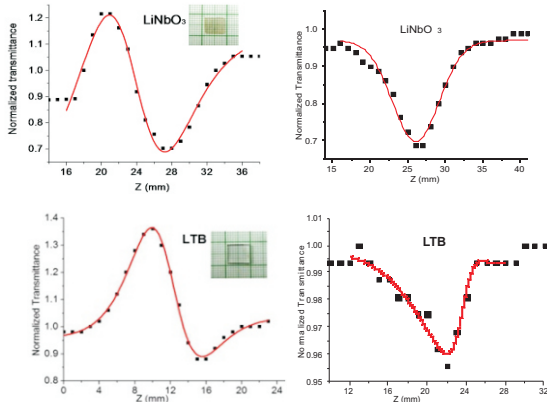


Fig. T.2.19: Open and closed aperture Z-scan for  $\text{LiNbO}_3$  (top row) and LTB (bottom row) crystals.

### 3.6 Holographic data storage properties of photorefractive crystals using two-wave coupling

Photorefractive crystals are useful for optical data storage device applications. Important properties of PR crystals, which decide its usability in data storage applications, are diffraction efficiency ( $\eta$ ), writing time ( $\tau_w$ ), erasure time ( $\tau_e$ ), dynamic range ( $M^{\#}$ ) and sensitivity ( $S$ ). A good PR material has high diffraction efficiency, small recording and erasure times, large dynamic range and high sensitivity. In order to measure PR properties of the congruent Lithium Niobate crystals grown in the Lab, a two-wave coupling experiment has been set up. Single doped  $\text{LiNbO}_3$  crystals have the limitation that the information recorded in them is volatile in nature, as it gets erased during the process of reading. Double doping of  $\text{LiNbO}_3$  offers the possibility of recording data in a non-volatile manner, because it has two different deep electron trap levels. The position of Fe trap level is slightly higher than that of Mn, as a result electrons are initially in the deeper trap and light of short wavelength transfers some of these electrons to the shallow trap via conduction band. This makes the recording of the holograms feasible using longer wavelength light. The final hologram is recorded in the deeper trap and therefore cannot be erased during the read-out

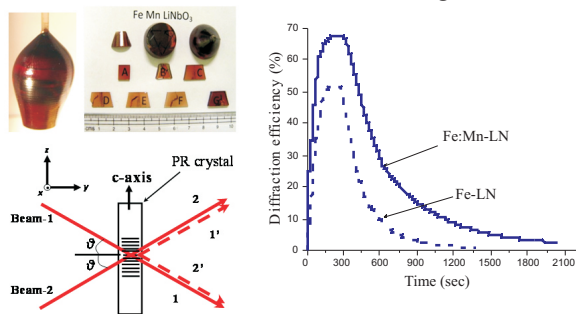


Fig. T.2.20: Two-wave coupling schematic and diffraction efficiency of  $\text{Fe}:\text{LiNbO}_3$  and  $\text{Fe}:\text{MnLiNbO}_3$ .

process. Figure T.2.20 shows the schematic of two-wave coupling phenomena and diffraction efficiency curves for single (Fe) and double doped (Fe,Mn) Lithium Niobate crystals [37]. Holographic data storage properties of the crystals are summarized in Table T.2.3. In addition, influence of proton exchange, annealing and different optical schemes on the holographic data storage properties of doped  $\text{LiNbO}_3$  crystals have been investigated [38, 39].

Table T.2.3: Holographic data storage properties of single and double doped lithium niobate crystals.

Crystal	Max. diff. efficiency ( $\eta_{max}$ ) (%)	Writing time ( $\tau_w$ ) (s)	Erasure time ( $\tau_e$ ) (s)	Dynamic range $M^{\#}$	Sensitivity $S$
Fe-LN	51.3	77	184	1.71	0.0366
Fe:Mn-LN	67.57	52.7	340	5.303	0.0445

## 4. X-ray techniques for characterizing defects in crystals

### 4.1 Imaging structural defects in crystals using x-ray topography (XRT)

Structural defects in single crystals, particularly the type of defects, the history of their generation and propagation during growth, has strong linkage with the quality of the grown crystal and their influence on the physical properties. In order to map spatial and temporal profile of defects in the crystals grown in the Lab, an x-ray topographic imaging facility has been established. It is based on the diffraction of x-rays by lattice planes satisfying the Bragg's condition. Around structural defect the planes are misoriented, resulting in low intensity of diffracted x-rays as compared to regions without (or less) defects. Thus a varying intensity contrast is recorded by the detector which represents the defect structure of the crystal under study. Figure T.2.21a shows the topograph of the bottom plate of flat-top KDP crystal [27]. It shows that dislocations originate from seed crystal and subsequently propagate into the bulk of the crystal. The topograph of the top plate (Figure T.2.21b) of the same crystal was found to have relatively lesser dislocations, indicating that the quality of crystal grown by flat-top methodology is comparable to those grown by conventional fast growth technology. Further, it is observed that the prismatic sector is more severely affected by dislocations as compared to pyramidal sector. Figure T.2.22 (a-c) show topographs of lithium iodate, lithium tetra borate and lithium niobate crystals having defects such as growth sector boundaries, striations, inclusion, dislocations and regions of misoriented lattice planes [40]. The defects state of each crystal was correlated with their optical properties. It was found that the optical properties such as optical transmission, refractive index homogeneity, laser damage threshold have significantly lower value for regions having higher defect density as compared to with lower defects density [27].

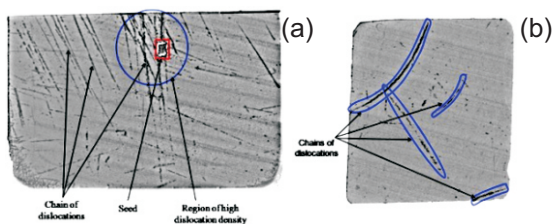


Fig. T.2.21: X-ray topograph of (316) planes in plates from (a) the bottom and (b) top of the flat-top KDP crystal.

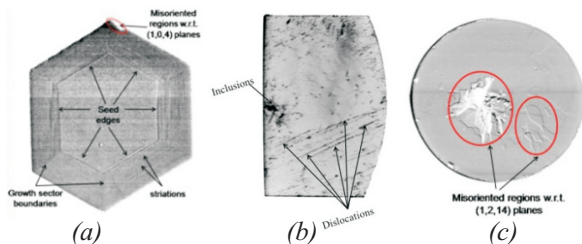


Fig. T.2.22: Topograph of (a) (104) planes in [001] oriented  $\text{LiIO}_3$  crystal, (b) (100) planes in [100] oriented  $\text{Li}_2\text{B}_4\text{O}_7$  crystal and (c) (1 2 14) planes in [001] oriented  $\text{LiNbO}_3$  crystal.

#### 4.2 Investigating crystalline perfection using high-resolution x-ray diffraction (HRXRD)

The crystalline perfection of the crystals was quantified by recording rocking curves using multi-crystal x-ray diffractometer in symmetrical Bragg geometry employing  $\text{MoK}\alpha_1$  radiation. Figure T.2.23a shows diffraction curve for a plate obtained from KDP crystal grown along phase matched direction [26]. The diffraction curve is sharp without any satellite peaks indicating that the crystalline perfection is very good without any internal grain boundaries. The FWHM of the diffraction curve is 15 arc-sec, which is very close to that expected from the plane wave theory of dynamical x-ray diffraction. The asymmetry in the diffraction curve is attributed to interstitial defects rather than vacancies, as the lattice around interstitial defect undergoes compressive stress and the inter-planer lattice spacing  $d$  decreases. Since  $d$  and  $\sin\theta_B$  are inversely proportional, it leads to higher scattering intensity at slightly higher Bragg angles ( $\theta_B$ ). Figure T.2.23b shows the rocking curve of sample taken from urea doped L-cysteine hydrochloride monohydrate crystal [41]. The solid line (convoluted curve) was fitted with the experimental data. On deconvolution of the diffraction curve, it was clear that the curve had an additional peak, which was 125 arc sec away from the higher intensity peak. The additional peak corresponds to an internal structural low angle grain boundary. The angular separation between the two peaks gives the tilt angle  $\alpha$  which is 66 arc s. The FWHM of the main peak and the low angle boundary are 35 and 110 arc s respectively.

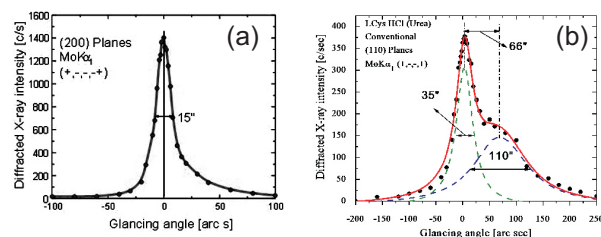


Fig. T.2.23: Diffraction curves recorded for (a) (200) diffracting planes of phase matched oriented KDP crystal, (b) (110) diffracting planes of urea doped L-cysteine hydrochloride monohydrate crystal.

#### 4.3 Quantifying metallic impurities in crystals using x-ray fluorescence (XRF)

X-ray fluorescence (XRF) is a non-destructive technique for identification and quantification of elemental composition of a sample. X-ray fluorescence beam-line (BL-16) of Indus-2 synchrotron radiation source was used for determination of metallic impurity distribution in a flat-top shaped KDP crystal. The x-ray fluorescence signal generated from the sample was collected by a CCD detector placed at  $90^\circ$  to the incident beam. Exposure time used was 1000 seconds in order to get sufficiently large signal from the impurities. The excitation wavelength selected using a monochromator was 10 keV because the binding energy of metallic impurities such as Fe, Ni, Cr etc. which are detrimental to the optical properties of KDP, lies below this value. The aim of the studies was to find the relative distribution of Fe and Ni impurities in the prismatic and the pyramidal growth sectors. The results show that pyramidal growth sector has lesser Fe impurity as compared to the prismatic growth sector. Additionally, it was found that the top plate had  $\sim 25\%$  lesser Fe concentration than the bottom plate. Figure T.2.24 shows the measured energy-dispersive x-ray fluorescence spectra showing chemical species in (001)-bottom plate of the FT-KDP crystal [27].

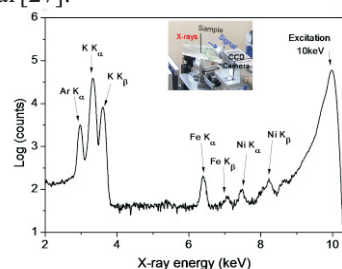


Fig. T.2.24: The measured energy-dispersive x-ray fluorescence spectra showing chemical species in (001)-bottom plate of the FT-KDP crystal.

#### Conclusion

In the first section, techniques for online and *in situ* optical imaging of the crystal growth process are presented and representative results for each have been discussed. In the

second part, optical techniques have been discussed for characterizing important figures of merit of crystals. Finally, x-ray techniques have been presented for characterizing the defects structure of single crystals.

### Acknowledgement

The author would like to express sincere thanks to Dr. K.S. Bartwal, Dr. Sujan Kar, Dr. S.K. Sharma, Shri C. Debnath and Shri Y.P. Singh for their contribution and help at various stages during the course of different studies reported here. Help received from Dr. M.K. Tiwari and Dr. G. Bhagvannarayana in XRF and HRXRD studies is gratefully acknowledged. Thanks are due to Dr. V.S. Tiwari and Dr. A.K. Karnal for useful advice and suggestions. Sincere gratitude is expressed to Shri S.V. Nakhe and Dr. P.A. Naik for encouragement and support.

### References

- [1] J.W. Mullin, Crystallization, 4<sup>th</sup> Edition, Butterworth-Heinemann, Oxford, 2001.
- [2] W.R. Wilcox, Prog. Cryst. Growth Charact. 26 (1993) 153-194.
- [3] F. Rosenberger and G. Muller, J. Cryst. Growth 65 (1983) 91-104.
- [4] Sunil Verma and Paul J. Shlichta, Prog. Cryst. Growth Charact. Materials 54 (2008) 1-120.
- [5] F. Mayinger, Optical Measurements: Techniques and Applications, Springer-Verlag, Berlin, 1994.
- [6] W. Schopf, J.C. Patterson and A.M.H. Brooker, Expts in Fluids 21 (1996) 331-340.
- [7] Sunil Verma, K. Muralidhar and V.K. Wadhawan, Ferroelectrics 323 (2005) 25-37.
- [8] Sunil Verma, Phase Transitions 83 (9) (2010) 714-727.
- [9] Sunil Verma, E. Depty and P.K. Gupta, 52<sup>nd</sup> DAE - SSPS, Univ. of Mysore, 2007.
- [10] Sunil Verma and K. Muralidhar, Recent Res. Develop. in Crystal Growth 5 (2009) 141-314.
- [11] S. Dinakaran, Sunil Verma, S.J. Das, S. Kar and K.S. Bartwal, Cryst. Res. Technol. 45 (2010) 233-238.
- [12] P.G. Vekilov, M. Ataka and T. Katsura, Acta. Cryst. D 51 (1995) 207-219.
- [13] Sunil Verma and K. Muralidhar, Opt. Las. Eng. 49 (2011) 915-923.
- [14] Sunil Verma, K. Muralidhar, Natl. Acad. Sci. Lett. 33 (5 & 6) (2010) 107-121.
- [15] Sunil Verma, J. Managre, C. Debnath, S. Kar, K.S. Bartwal, V.S. Tiwari, A.K. Karnal, Proc. 27<sup>th</sup> National Laser Symposium, 3-6 Dec. 2018, RRCAT Indore.
- [16] J.M. Mehta, Appl. Opt. 29 (13) (1990) 1924-1932.
- [17] C.S. Vikram and W.K. Witherow, Exp. Mech. (March 1992) 74-77.
- [18] C.S. Vikram, W.K. Witherow and J.D. Trolinger, Appl. Opt. 31 (1992) 7249-7252.
- [19] G.T. Herman, Image Reconstruction from Projections: The Fundamentals of Computerized Tomography, Academic Press, New York, 1980.
- [20] R.M. Lewitt, IEEE 71 (1983) 390-408.
- [21] Y. Censor, IEEE 71 (1983) 409-419.
- [22] Sunil Verma, K. Muralidhar and V.K. Wadhawan, in Computerized Tomography for Scientists and Engineers, P. Munshi (Editor), CRC Press, New York, 2006, pp. 158-174.
- [23] Sunil Verma and K. Muralidhar, in: CT2008: Tomography Confluence, P. Munshi (Editor) Amer. Inst. of Phys. CP 1050, Melville, New York, 2008, pp. 103-114.
- [24] S. Dinakaran, Sunil Verma, S. Jerome Das, S. Kar and K.S. Bartwal, Physica B 405 (2010) 3919-3923.
- [25] S. Dinakaran, Sunil Verma, S. Jerome Das, S. Kar, K.S. Bartwal and P.K. Gupta, Physica-B 405 (2010) 1809-1812.
- [26] S. Dinakaran, Sunil Verma, S. Jerome Das, G. Bhagavannarayana, S. Kar and K.S. Bartwal, Appl. Phys. A 99 (2) (2010) 445-450.
- [27] S.K. Sharma, Sunil Verma, Yeshpal Singh, K.S. Bartwal, M.K. Tiwari, G.S. Lodha, G. Bhagavannarayana, Opt. Mater. 46 (2015) 329-338.
- [28] Sunil Verma, S. Kar and K.S. Bartwal, Chapter 19, in: "Interferometry Principles and Applications", M.E Russo (Editor), 2012, 537-560, (Nova Science Publishers, New York, USA).
- [29] S. Kar, Sunil Verma, M.S. Khan and K.S. Bartwal, Cryst. Res. Technol. 44 (12) (2009) 1303-1307.
- [30] S. Dinakaran, Sunil Verma, S. Jerome Das, G. Bhagavannarayana, S. Kar and K.S. Bartwal, Appl. Phys. B 103 (2011) 345-349.
- [31] S. Kar, Sunil Verma and K.S. Bartwal, Cryst. Growth Des., 8 (12) (2008) 4424-4427.
- [32] S. Kar, Sunil Verma and K.S. Bartwal, Cryst. Res. Technol., 44 (3) (2009) 305-308.
- [33] S. Kar, Sunil Verma and K.S. Bartwal, Cryst. Res. Technol., 43 (4) (2008) 438-442.
- [34] S. Dinakaran, Sunil Verma and S. Jerome Das, Cryst Eng Comm 13 (2011) 2375-2380.
- [35] M. Sheik-Bahae, A.A. Said and E.W. Van Stryland, IEEE J. of Quantum Electron. 26(4) (1990) 760-769.
- [36] B.R. Sharma, M. Tech. thesis (2016), SGSITS & RRCAT, Indore.
- [37] Sunil Verma, S. Kar, K.S. Bartwal and P.K. Gupta, Proc. 19<sup>th</sup> National Laser Symposium, 1-4 Dec. 2010, RRCAT, Indore.
- [38] S. Kar, Sunil Verma, M.W. Shaikh and K.S. Bartwal, Physica-B 404 (20) (2009) 3507-3509.
- [39] Sunil Verma, Vinoth V., S. Kar, C. Debnath, K.S. Bartwal and P.K. Gupta, Proc. 24<sup>th</sup> National Laser Symposium, 2-5 Dec. 2015, RRCAT, Indore.
- [40] Sunil Verma, S.K. Sharma and K.S. Bartwal, RRCAT Newsletter 26(2) (2013) 26.
- [41] Sunil Verma, K.R. Rao, S. Kar, K.S. Bartwal, Spectrochimica Acta - Part A: Molecular and Biomolecular Spectroscopy 153 (2016) 16-21.